

BCSJ Award Article**Three Structural Isomers of Dinaphthothieno[3,2-*b*]thiophenes: Elucidation of Physicochemical Properties, Crystal Structures, and Field-Effect Transistor Characteristics**Tatsuya Yamamoto,^{1,†} Shoji Shinamura,¹ Eigo Miyazaki,¹ and Kazuo Takimiya^{*1,2}¹Department of Applied Chemistry, Graduate School of Engineering, Hiroshima University, Higashi-Hiroshima 739-8527²Institute for Advanced Materials Research, Hiroshima University, Higashi-Hiroshima 739-8530

Received September 1, 2009; E-mail: ktakimi@hiroshima-u.ac.jp

In order to gain an insight into the relationship between the molecular structure and the semiconductor characteristics of highly π -extended heteroarene-based organic semiconductors, three structural isomers of dinaphthothieno[3,2-*b*]thiophenes with C_{2h} symmetry were investigated. Of these, two isomers, dinaphtho[2,1-*b*:2',1'-*f*]thieno[3,2-*b*]thiophene (**2**) and dinaphtho[1,2-*b*:1',2'-*f*]thieno[3,2-*b*]thiophene (**3**), were newly synthesized, characterized, and utilized as active semiconducting layers in organic field-effect transistors (FETs). Detailed investigation of the physicochemical properties of **2** and **3**, together with another isomer, dinaphtho[2,3-*b*:2',3'-*f*]thieno[3,2-*b*]thiophene (**1**), indicated that the electronic structures of the three isomers are fairly different from each other despite having the same molecular formula and the same aromatic constituents. Comparison of the molecular arrangements in the crystals elucidated by X-ray structural analysis implied that the molecular shape and the thus-induced favorable intermolecular interactions play important roles in determining the entire molecular arrangement. The characteristics of **2**- and **3**-based FETs with maximum field-effect mobilities (μ_{FETS}) of 10^{-3} – 10^{-2} cm² V⁻¹ s⁻¹ were inferior to those of **1**-based FETs with μ_{FETS} up to 3.0 cm² V⁻¹ s⁻¹. The inferior characteristics of **2**- and **3**-based devices were due to film morphology as elucidated by atomic force microscopy (AFM) and supported by theoretical calculations of electronic structure in the solid state. Together, the results indicate that the molecular structure and shape, even for similar heteroarenes with the same molecular formula and symmetry, are important parameters to determine the solid-state properties of organic semiconductors.

Pentacene, a representative oligoacene consisting of five benzene rings fused in a linear manner, is widely utilized as a standard organic semiconductor for high-performance thin-film-based organic field-effect transistors (OFETs) showing field-effect mobilities (μ_{FETS}) higher than 1.0 cm² V⁻¹ s⁻¹.¹ Higher oligoacenes than pentacene, e.g., hexacene that has six fused benzene rings, are promising candidates for the development of superior organic semiconductors that show better performance than pentacene.² However, the instability of such large oligoacenes has hindered their practical use as an organic semiconductor.³

In sharp contrast, we recently reported that a newly developed highly π -extended heteroarene, dinaphtho[2,3-*b*:2',3'-*f*]thieno[3,2-*b*]thiophene (DNNT, **1**), which possesses six aromatic rings fused in a linear manner, is stable and its evaporated thin-film-based OFETs show μ_{FETS} as high as

3.0 cm² V⁻¹ s⁻¹.⁴ The stabilization of the heteroarene can be understood by lowering the energy levels of the highest occupied molecular orbital (HOMO) and raising the energy levels of the lowest unoccupied molecular orbital (LUMO), resulting in a large HOMO–LUMO energy gap.⁵ The high stability and good performances of DNNT-based OFETs indicate that the introduction of the thieno[3,2-*b*]thiophene substructure into the acene framework is beneficial for the development of new organic semiconductors based on highly π -extended aromatic compounds.

The molecular structure of **1** can be viewed as a benzo-fused [1]benzothieno[3,2-*b*][1]benzothiophene (BTBT) or a naphtho-fused thieno[3,2-*b*]thiophene with C_{2h} symmetry. Using the same aromatic constituents, one can draw two structural isomers while keeping the same symmetry, namely, dinaphtho[2,1-*b*:2',1'-*f*]thieno[3,2-*b*]thiophene (**2**) and dinaphtho[1,2-*b*:1',2'-*f*]thieno[3,2-*b*]thiophene (**3**)⁶ (Figure 1). Although the isomers have the same aromatic constituents, their molecular shapes and electronic structures are expected to differ.

[†] Present address: Research Center for Composite Device Technology, Iwate University, Hanamaki 025-0312

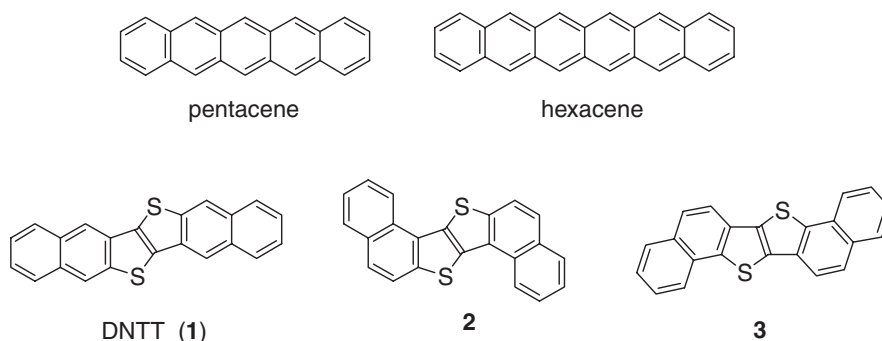
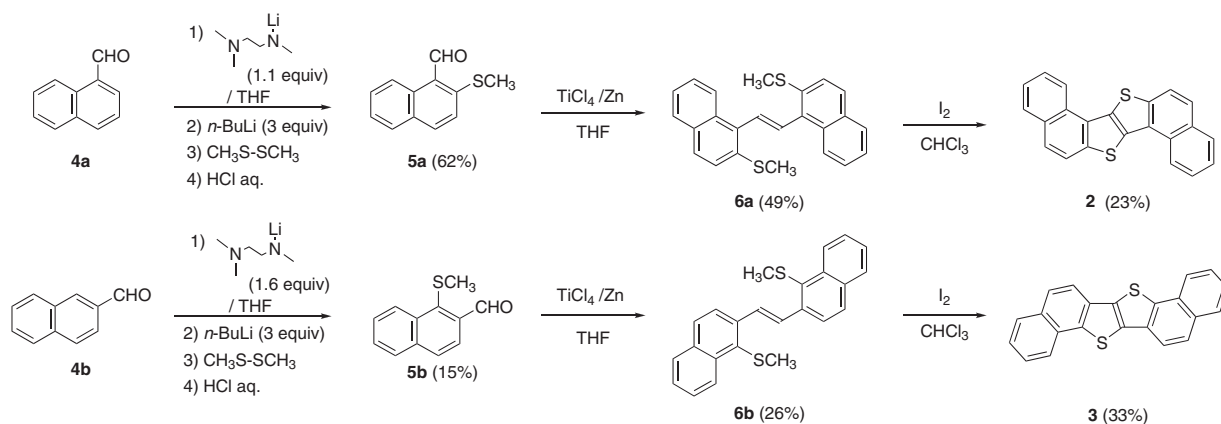


Figure 1. Chemical structures of highly extended acenes and heteroarenes.



Scheme 1. Synthesis of **2** and **3**.

Furthermore, the difference in molecular shape will bring about different molecular arrangements in the solid state, and this will have a significant impact on the electrical properties in the solid state, including the FET characteristics of thin-film-based devices. Keeping these expectations in mind, we carried out the syntheses, characterization, and elucidation of the crystal structures of isomers **2** and **3**, as well as the evaluation of FET characteristics of evaporated thin-film-based OFET devices. Comparison of **1–3** in terms of molecular factors, i.e., molecular and electronic structure, frontier orbitals, reorganization energy, and intermolecular factors, i.e., molecular arrangement in the solid state and intermolecular transfer integrals, will give an insight into understanding molecular design strategies for superior organic semiconductors. We here report the synthesis, characterization, crystal structures, and FET characteristics of evaporated thin-film-based OFETs, together with theoretical studies of the electronic structures of **1–3** in the solid state.

Results and Discussion

Synthesis. DNTT isomers **2** and **3** were synthesized following a three-step procedure similar to that reported for the synthesis of **1** (Scheme 1).^{4a} Commercially available 1- or 2-naphthaldehyde as starting material was first ortho-lithiated using excess butyllithium in the presence of *N,N,N'*-trimethylethylenediamine in THF,⁷ and the resulting lithium naphthalenide intermediates were reacted with dimethyl disulfide to give corresponding naphthaldehyde with a methylthio group at the ortho-position. Although the desired 2-methylthio-1-naphthaldehyde (**5a**)⁸ was selectively obtained when 1-naphthalde-

hyde (**4a**) was the substrate, the same procedure applied to 2-naphthaldehyde (**4b**) gave a mixture of isomers consisting of desired 1-methylthio-2-naphthaldehyde⁹ (**5b**, 15% yield) and 3-methylthio-2-naphthaldehyde (58% yield), the latter of which is the intermediate for **1**. Aldehydes **5a** and **5b** were readily converted into olefinic intermediates **6a** and **6b** in moderate yields by low-valent titanium-mediated olefination.¹⁰ The conversion of **6a** and **6b** into **2** and **3**, respectively, which was accomplished by the action of I₂ in refluxing CHCl₃, was readily achieved, although the conversion yields were low. Compounds **2** and **3** were fully characterized by spectroscopic and combustion elemental analyses, and the selective formation of **2** and **3** was unambiguously confirmed by X-ray single crystal analyses (vide infra).

Electrochemical and Spectroscopic Properties. The oxidation potentials of isomers **1–3** determined by cyclic voltammetry are summarized in Table 1, together with spectroscopic data extracted from UV-vis spectra (Figure 2).

The first oxidation potentials of **2** (+0.83 V, vs. ferrocene/ferrocenium) and **3** (+0.87 V) are slightly higher than that of **1** (+0.75 V), which means that the HOMO energy levels of **2** and **3** are lower than that of **1**. The HOMO energy levels estimated from the oxidation onsets are 5.44 eV for **1**, 5.54 eV for **2**, and 5.58 eV for **3** below the vacuum level,¹¹ and are higher than that of BTBT (5.74 eV) that corresponds to the common central core structure of **1–3**, indicating that the π -system extension contributes to the elevation of HOMO energy level, although the perturbation effect depends on the position of attachment of the outermost benzene rings.

In accordance with the elevation of HOMO energy levels caused by the addition of two benzene rings to the BTBT core, HOMO–LUMO gaps optically estimated as well as the LUMO energy levels of **1–3** are decreased. However, the extent of LUMO energy level lowering is not consistent in **1–3**: pronounced lowering of LUMO energy level and the HOMO–LUMO gap is noticeable in **1**, in which the additional benzene ring is fused in a linear manner.

MO Calculations. To elucidate the dependence of the perturbation effect of the outermost benzene rings on the annulated positions in the BTBT core structure, we carried out MO calculations with the DFT method at the B3LYP/6-31G(d) level using Gaussian03 program.¹² HOMO and LUMO of **1–3**

Table 1. Electrochemical and UV–Vis Data of **1–3** and Thus-Estimated HOMO and LUMO Energy Levels

	$E_{\text{ox}}^{\text{a)}}$ / V $E_{1/2}$ /onset	$\lambda_{\text{max}}^{\text{b)}}$ / nm peak/edge	HOMO ^{c)} /eV	$E_{\text{g}}^{\text{d)}$ /eV	LUMO /eV
1	+0.75/+0.64	401/420	−5.44	2.95	−2.49
2	+0.83/+0.74	367/380	−5.54	3.26	−2.28
3	+0.87/+0.78	351/370	−5.58	3.35	−2.23
BTBT ^{e)}	+1.02/+0.94	332/345	−5.74	3.59	−2.15

a) Versus Fc/Fc⁺. b) Absorption spectra. c) Estimated from the onset of the oxidation peak. d) Determined from the absorption edge. e) [1]Benzothieno[3,2-*b*][1]benzothiophene.

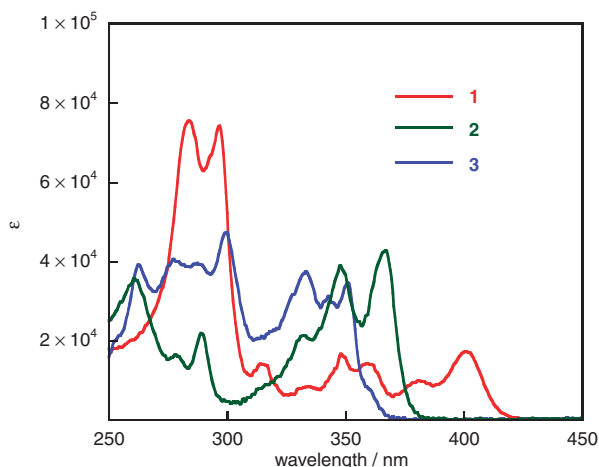


Figure 2. UV–vis spectra of **1–3** in CH₂Cl₂.

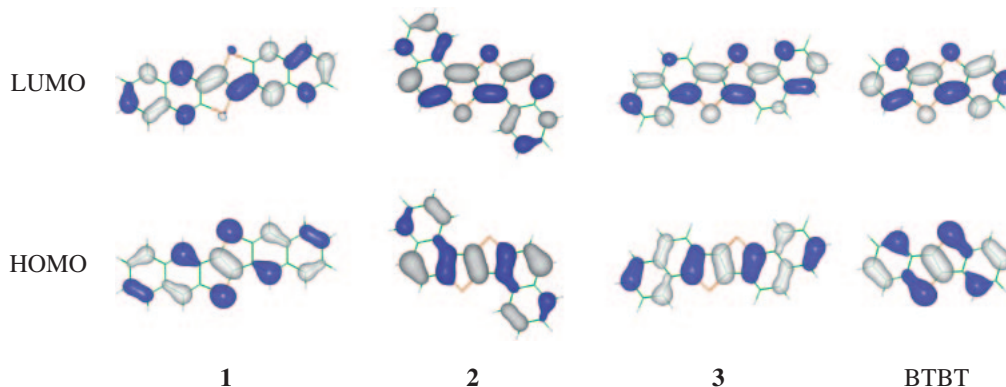


Figure 3. Calculated frontier orbitals of **1–3** and BTBT.

and BTBT are depicted in Figure 3, and the calculated energy levels of their frontier orbitals are listed in Table 2. The experimentally estimated energy levels listed in Table 1 are qualitatively reproduced by the theoretical calculations, indicating that the calculations are useful to understand the difference in electronic structure among the isomers.

Regardless of the isomer, the coefficients (charge densities) of both HOMO and LUMO spread over the entire molecular framework. In other words, effective conjugation is extended to the outermost benzene rings. The distribution of coefficients of HOMO, on the other hand, is quite different among the isomers (Figure 3). Focusing on the central BTBT core structure in **1–3**, HOMO of **1** can be understood as a linear combination of HOMOs of BTBT and 1,3-butadiene, resulting in a partially acene-like electronic structure, i.e., half of the molecule, the naphtho[3,2-*b*]thiophene moiety, is isoelectronic with anthracene. In sharp contrast, HOMOs of **2** and **3** do not preserve the features of the BTBT core structure, thereby resulting in a very different electronic system from that of **1**, which may be reflected by the fact that the naphthothiophene moieties in these compounds are isoelectronic with phenanthrene. These considerations based on MO calculations indicate that the perturbation effect of the outermost benzene rings is not just a simple π -extension, and that the properties of **2** and **3** as a p-channel organic semiconductor will be different from those of **1**.

We also computed the internal reorganization energy for hole (λ^{h}) for **1–3**, since the internal reorganization (λ) and the intermolecular transfer integral (t) are important factors for the carrier transport under the hopping transport mechanism, which is believed to be important for thin-film OFETs.¹³ According to Marcus theory,^{13,14} the rate of charge transfer between two identical molecules, k_{ct} , depends on λ and t :

Table 2. Calculated HOMO and LUMO Energy Levels and Reorganization Energy for Hole of **1–3** and BTBT with the DFT Method at the B3LYP/6-31G(d) Level

	HOMO /eV	LUMO /eV	λ^{h} /eV
1	−5.18	−1.81	0.130
2	−5.32	−1.61	0.199
3	−5.47	−1.46	0.192
BTBT	−5.58	−1.26	0.226

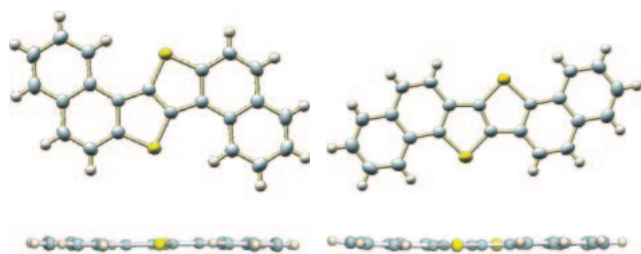


Figure 4. Molecular structures of **2** (left) and **3** (right).

$$k_{\text{ct}} = (t^2/h)(\pi/\lambda k_{\text{B}}T)^{1/2} \exp(-\lambda/4k_{\text{B}}T) \quad (1)$$

where h is Planck constant, k_{B} Boltzmann constant, and T the temperature.

As summarized in Table 2, all **1–3** molecules have smaller λ^{h} s than that of BTBT. This agrees well with the general tendency between the extension of π -conjugation system and the reorganization energies: with extension of π -conjugation system, smaller λ is realized.¹⁵ On the other hand, comparison of **1–3** indicates that **1** has apparently smaller λ^{h} than those of **2** and **3** by more than 60 meV. This can be qualitatively explained by the electronic structure of their HOMOs. As discussed above, only **1** has a partially acene-like electronic structure, whereas **2** and **3** have a phene-like one. The phene-substructure can be energetically stabilized by localized aromatic nature at the neutral state, whereas injection of cationic charge requires large deformation of molecular structure, which results in large λ^{h} for **2** and **3**. On the other hand, the acene-like electronic structure in **1** receives little stabilization effect from the localized aromaticity at the neutral state, and thus the deformation of molecular structure at the cationic state is rather smaller than those of **2** and **3**.

X-ray Single Crystal Analysis. Since the molecular arrangement in the solid state influences the electronic properties of organic semiconductors in the condensed phase, elucidation of the exact molecular and crystal structures by means of X-ray single crystal analysis is vital. As we already reported, the molecular arrangement in the crystal of **1** is characterized by herringbone packing (Figure S1),^{4a} which is known to be the optimal molecular arrangement for high-performance OFET materials, as can be seen for pentacene.¹⁶ The molecular and crystal structures of **2** and **3** determined in the present work are depicted in Figure 4 and Figure 5, respectively. Both molecules are almost completely planar with maximum deviation from the mean plane of 0.0179 Å for **2** and 0.0458 Å for **3** (Figure 4).

As in the case of **1**, both **2** and **3** assume a layer-by-layer crystal structure, although the crystallographic axis that the layers pile up along is different: the crystallographic c axis direction for **1** (Figure S1), and the a axis direction for **2** and **3** (Figure 5). The molecular arrangement of **2** and **3** in their respective layers however, is strikingly different from that of **1** and also different from each other. **2** takes a simple π -stack structure (Figure 5a), whereas **3** assumes the so-called sandwich herringbone in which dimers of **3** are packed in a herringbone manner (Figure 5b).

Although it is difficult to rationalize the crystal structure differences among the isomers, we speculate that the molecular shape and the thus-induced preferred intermolecular interac-

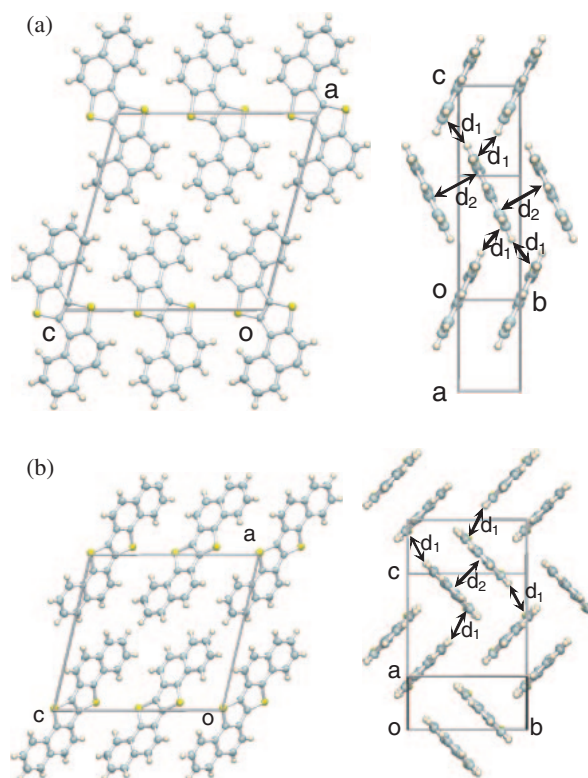


Figure 5. Crystal structures of **2** (a) and **3** (b). Intermolecular distances: $d_1(\text{S}\cdots\text{H}) = 3.037 \text{ \AA}$, $d_2(\pi\cdots\pi) = 3.536 \text{ \AA}$ for **2**; $d_1(\text{C}\cdots\text{H}) = 2.861$ and 2.866 \AA , $d_2(\pi\cdots\pi) = 3.434 \text{ \AA}$ for **3**.

tions may play a critical role.¹⁷ For linear isomer **1** with a partially acene-like structure, the herringbone packing is favorable as seen in the crystal structures of oligoacenes. In contrast, for markedly bent, S-shaped **2**, the herringbone structure seems to be less favorable because of the lack of hydrogen atoms suitable for the face-to-edge CH- π interaction. Thus, the optimal intermolecular interaction of **2** is the face-to-face manner, resulting in the π -stack structure. In contrast, **3** with a slightly bent molecular structure corresponds to an intermediate between **1** and **2**: the crystal structure of **3** is understood from the coexistence of two different intermolecular interactions, the face-to-face π -stacking forming the dimer structure and the face-to-edge CH- π interactions resulting in the sandwich herringbone.

Detailed inspection of the crystal structures of **2** and **3** suggests that the above consideration may be adequate. In the crystal structure of **2**, the intermolecular face-to-face distance in the π -stacks is 3.536 Å, which is almost the same as the reported value of the sum of van der Waals radii of π -electrons (3.536 Å).¹⁸ However, no close contact between the π -stacks is noted, indicating that the structure of **2** is highly one-dimensional (1D). In contrast, very short face-to-face distances were observed for the dimer of **3** (d_2 in Figure 5, 3.434 Å), and the inter-dimer C-H distances are 2.861 and 2.866 Å, shorter than the sum of van der Waals radii of carbon and hydrogen atoms (2.90 Å).¹⁸ It is reasonable to consider that these two kinds of close intermolecular interactions play a substantial role in **3** to take the sandwich herringbone structure.

Vapor-Deposited Thin Films. Homogeneous thin films of **2** and **3** with metallic luster were prepared by physical vapor deposition on n-doped Si wafer with 200 nm thermally grown SiO₂ that was surface-modified with octyltrichlorosilane (OTS)¹⁹ or hexamethyldisilazane (HMDS).²⁰ The deposition of thin films of **3** was successful at any substrate temperatures during deposition (T_{sub} , rt, 60 or 100 °C), whereas no thin film of **2** was obtained at $T_{\text{sub}} = 100$ °C, probably owing to the high volatility of **2**, which causes re-sublimation on the surface of the substrate at 100 °C.

Figures 6 and 7 show AFM images of vapor-deposited thin films of **2** and **3** on HMDS-modified substrates, respectively. The surface morphology of the thin film of **2** was fairly affected by T_{sub} : at $T_{\text{sub}} = \text{rt}$, the film consisted of small crystalline

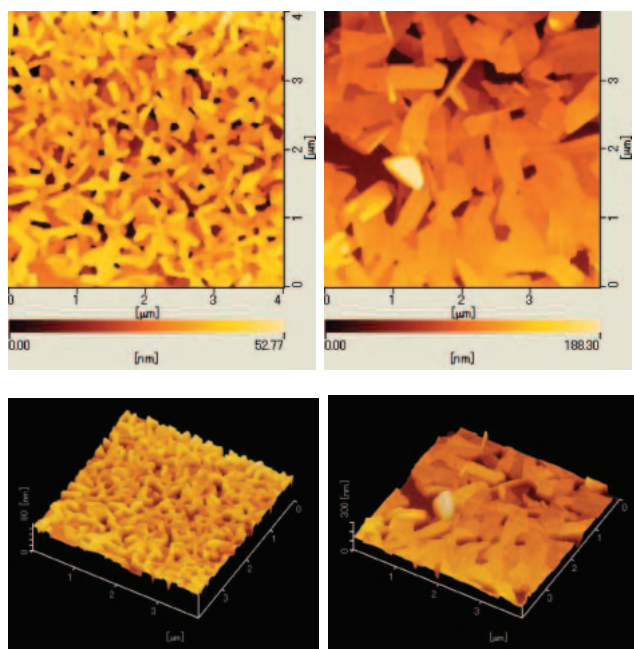


Figure 6. AFM images of evaporated thin films of **2**: $T_{\text{sub}} = \text{rt}$ (left) and 60 °C (right).

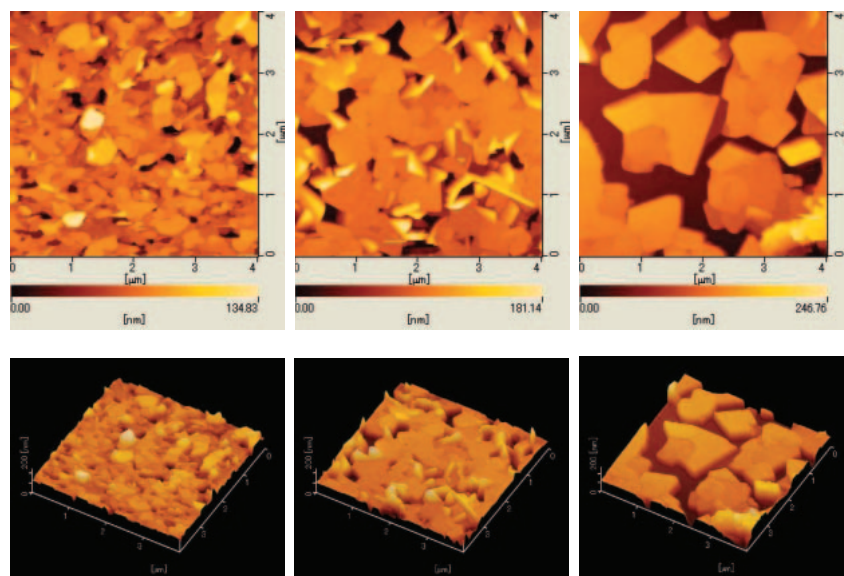


Figure 7. AFM images of evaporated thin films of **3**: $T_{\text{sub}} = \text{rt}$ (left), 60 °C (center), and 100 °C (right).

grains with needle-like shape, whereas at $T_{\text{sub}} = 60$ °C relatively large grains (ca. 1 μm in size) were observed. The surface morphology of the thin film of **3** was also affected by T_{sub} : at $T_{\text{sub}} = \text{rt}$, the film consisted of small crystalline grains of sub-micrometer size. In contrast, in the film deposited at $T_{\text{sub}} = 100$ °C, plate-like crystalline grains larger than 1 μm in size were observed. This may be related to the crystalline phase at $T_{\text{sub}} = 100$ °C determined by XRD measurements, as we will discuss later.

The size of crystalline grains in the thin films of **2** and **3** depended markedly on T_{sub} , and a similar T_{sub} dependence of grain size was also observed for the vapor-deposited films of **1** (Figure S2). However, the shape of the crystalline grains was primarily dependent on the type of compound. Needle-like and plate-like crystalline grains were observed for **2** and **3**, respectively, whereas a dendritic texture reminiscent of pentacene thin films²¹ was observed for **1**-based thin film at $T_{\text{sub}} = 100$ °C on the HMDS-treated substrate (Figure S2). From these observations, we speculate that the effects of the number of grain boundaries are similar to each other, although the nature of the grain boundaries, in other words, connectivity between grains, may be different for each compound.

XRDs of Evaporated Thin Films. Figure 8 shows the X-ray diffraction (XRD) patterns of the thin films on HMDS-modified Si/SiO₂ substrates. Irrespective of T_{sub} , the XRD patterns of the thin films of **2** are identical and can be well characterized by the simulated powder pattern of bulk single crystal (Figure 9a). Two intense peaks ($2\theta = 6.5$ and 19.5°) are assigned to (100) and (300) diffractions, indicating that the crystallographic a axis is perpendicular to the substrate. Thus, the crystallographic bc plane (Figure 5a) is expected to be parallel to the substrate, that is, the molecular arrangement is closely related to carrier transport in FET devices.

The XRD patterns of the thin films of **3** show the coexistence of two different phases, the major phase in each pattern depending on T_{sub} . By comparing the simulated powder patterns of **3** based on the single crystal structure (Figure 9b), the major phase at $T_{\text{sub}} = 100$ °C with monolayer thickness

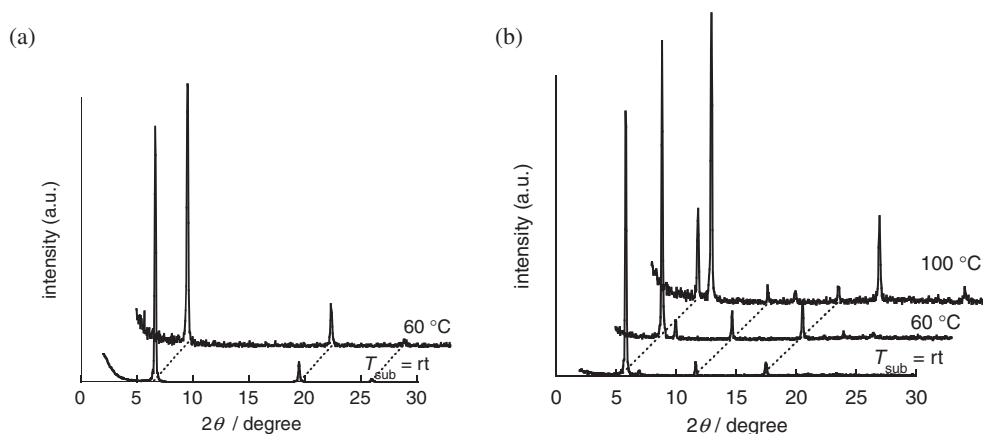


Figure 8. XRD patterns of **2**-based (a) and **3**-based (b) thin films on HMDS-modified substrates.

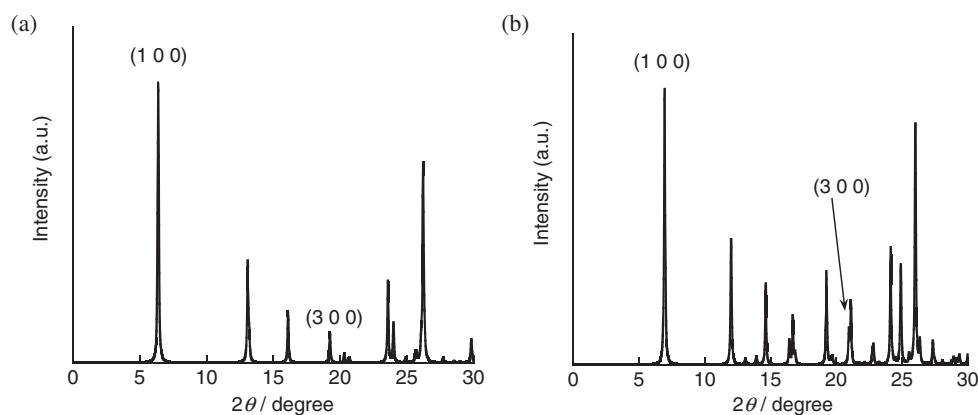


Figure 9. Simulated powder patterns of **2** (a) and **3** (b) based on X-ray single crystal structures.

(d -spacing) of 12.6 \AA was assigned to the bulk single crystal phase. Two intense peaks at $2\theta = 7.0$ and 21.0° correspond to (100) and (300) reflections, respectively, showing that the crystallites of **3** in the thin film perpendicular orient with the crystallographic a axis to the substrate. The crystallographic bc plane (Figure 5b) is thus parallel to the substrate, which is actually the channel direction in FET devices as seen in the thin film of **2**.

In contrast, the other phase detected as the major phase at $T_{\text{sub}} = \text{rt}$ has longer d -spacing (15.0 \AA) than that of the bulk single crystal phase, which is close to the molecular length of **3** (ca. 14.9 \AA). Thus, in the present phase (thin-film phase), the molecules of **3** are nearly perpendicular to the substrate, different from the bulk single crystal phase. However, the FET characteristics of devices fabricated from the thin film of **3** deposited at $T_{\text{sub}} = \text{rt}$ are more or less similar to those deposited at different T_{sub} (vide infra).

OFET Devices. Fabrication of OFET devices was completed by the deposition of source and drain electrodes on top of evaporated thin films of **2** or **3** through a shadow mask. Thus-obtained devices having a “top-contact” configuration with $W/L = \text{ca. } 30$ were evaluated in ambient conditions and found to exhibit typical p-channel FET characteristics, as shown in Figure 10. Table 3 summarizes the FET characteristics of **2**- and **3**-based OFET devices. In contrast to the impressive performance of **1**-based OFETs showing μ_{FETS} as high as $3.0 \text{ cm}^2 \text{ V}^{-1} \text{ s}^{-1}$ with current on/off ratio ($I_{\text{on}}/I_{\text{off}}$) of

$10^{7,4}$ the performance of **2**- and **3**-based OFETs is rather inferior. For **2**-based devices, μ_{FETS} are in the order of $10^{-2} \text{ cm}^2 \text{ V}^{-1} \text{ s}^{-1}$, and for **3**-based devices, they are in the order of $10^{-3} \text{ cm}^2 \text{ V}^{-1} \text{ s}^{-1}$.

The present devices showed not only mobilities that were lower by two or three orders of magnitude than those of **1**-based OFETs, but higher threshold voltages (V_{th} s) as well. Although V_{th} is not purely a molecular property but one of the device characteristics influenced by both factors in the device configuration and properties of the materials used, the high V_{th} of **2**- and **3**-based OFETs can be related to the lower HOMO energy levels of **2** and **3** than that of **1** (ca. $9 \pm 4 \text{ eV}$).

Another point that should be addressed is the weak T_{sub} dependence of FET characteristics. For **3**-based devices, in particular, the existence of different phases depending on T_{sub} s was confirmed by XRD analyses. However, the μ_{FETS} of devices fabricated at $T_{\text{sub}} = 100^\circ \text{C}$, in which the bulk single crystal phase is dominant, are almost the same as those of devices fabricated at lower T_{sub} . The reasons for the weak T_{sub} dependence of FET characteristics are not known at the moment.

Electronic Structures of 1–3 in the Solid State. The FET characteristics of the devices are affected by several factors, including the electronic structure of an individual molecule, the molecular arrangement in the thin-film state, grain boundaries in the channel, and interfacial morphology between the organic semiconductor and the gate dielectric. Among such factors, the effects from the molecular arrangement in the thin-film state, in

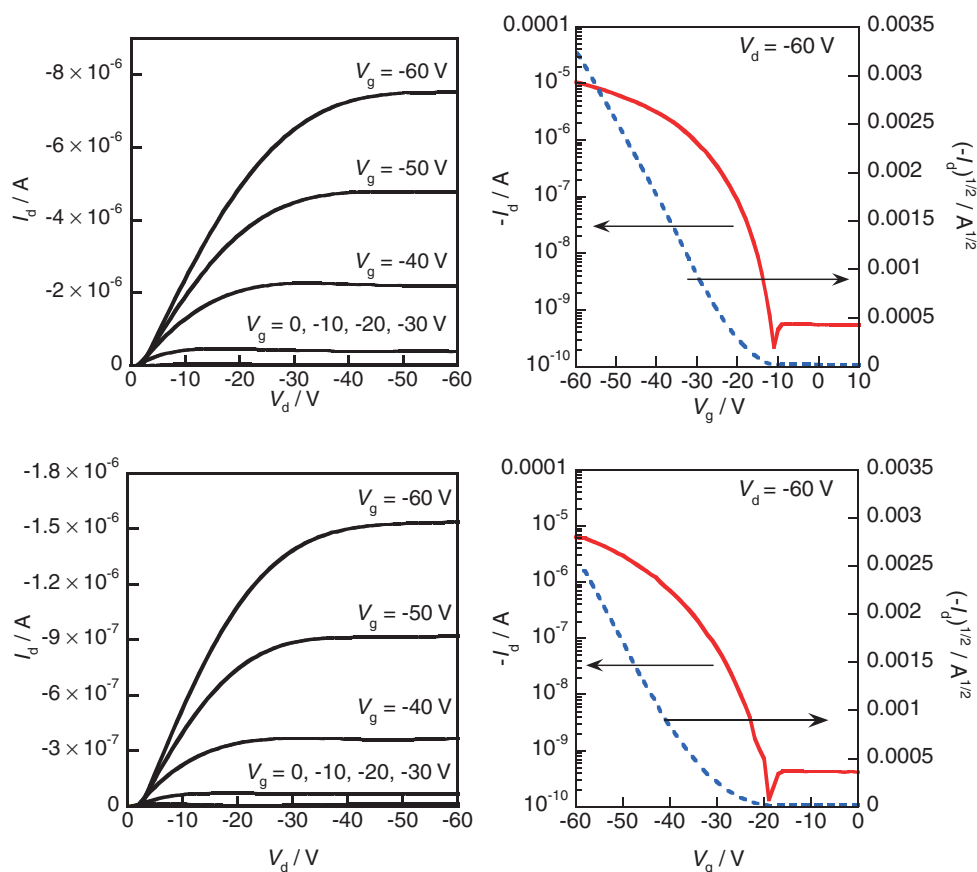


Figure 10. Output (left) and transfer characteristics (right) of **2**-based (upper) and **3**-based (lower) devices with OTS modification and $T_{\text{sub}} = \text{rt}$.

Table 3. FET Characteristics of **2**- and **3**-Based Devices Fabricated on Si/SiO₂ Substrates with Different Surface Treatments and under Different Substrate Temperatures (T_{sub})

Surface-treatment reagent	$T_{\text{sub}} / ^\circ\text{C}$	$\mu_{\text{FET}}^{\text{a)}$ / $\text{cm}^2 \text{V}^{-1} \text{s}^{-1}$	$I_{\text{on}}/I_{\text{off}}$	V_{th}/V	
2 HMDS	rt	$1.0\text{--}1.2 \times 10^{-2}$	10^4	-12 ± 2	
	60	$0.92\text{--}1.1 \times 10^{-2}$	10^3	-13 ± 4	
	OTS	rt	$1.2\text{--}2.3 \times 10^{-2}$	5×10^4	-14 ± 3
		60	$0.95\text{--}2.6 \times 10^{-2}$	10^4	-15 ± 5
3 HMDS	rt	$3.2\text{--}3.6 \times 10^{-3}$	10^3	-14 ± 3	
	60	$2.8\text{--}3.1 \times 10^{-3}$	5×10^3	-13 ± 2	
	100	$4.8\text{--}7.4 \times 10^{-3}$	10^4	-27 ± 3	
	OTS	rt	$3.8\text{--}7.4 \times 10^{-3}$	10^5	-24 ± 2
		60	$2.2\text{--}8.6 \times 10^{-3}$	5×10^3	-28 ± 5
		100	$1.4\text{--}2.6 \times 10^{-2}$	5×10^4	-33 ± 5

a) Data from more than 10 devices.

particular, the intermolecular electronic coupling is one of the most important, according to Marcus theory.^{13,14}

In order to evaluate intermolecular electronic coupling more quantitatively, calculation of transfer integrals between HOMOs of molecules **1**–**3** in the semiconducting layer elucidated by X-ray analyses were carried out using the Amsterdam Density Functional (ADF) program package.^{13e,22,23} Calculated transfer

integrals between HOMOs are shown in Figure 11. For **1** that gives superior FET performance (Figure 11a), both the transfer integral along the stacking direction designated as t_a and those in the side-by-side direction (designated as t_p and t_q) are large up to 91 meV, clearly indicating that a two-dimensional (2D), strongly interactive electronic structure is realized. On the other hand, the calculated transfer integrals of **2** (Figure 11b) indicate that the electronic structure is highly one-dimensional (1D): the transfer integral along the stacking direction (designated as t_b) is large (ca. 35 meV), but that in the side-by-side direction (t_p) is less than one-tenth (ca. 2.0 meV) of t_b . It is thus understood that the lack of a 2D interactive structure is one of the reasons for the inferior transport characteristics of **2**-based FETs compared to those of **1**-based devices.

The distribution of the calculated transfer integrals of **3** with the sandwich herringbone structure (Figure 11c) is rather complicated, and it shows characteristic features of the structural type. The transfer integral between HOMOs in the dimers is very large ($t_p = 172$ meV) compared to those of other inter-dimer modes. Small but similar magnitude of inter-dimer transfer integrals both in the crystallographic a ($t_{q2} = 6.0$ meV) and b ($t_b = 2.0$ meV) directions suggests that weakly interactive 2D electronic structure is plausible for the molecular packing of **3** in the crystal. Thus, the poor transport characteristics of **3**-based FETs can be explained by the weak orbital coupling between the dimers, although the intra-dimer orbital coupling is very strong.

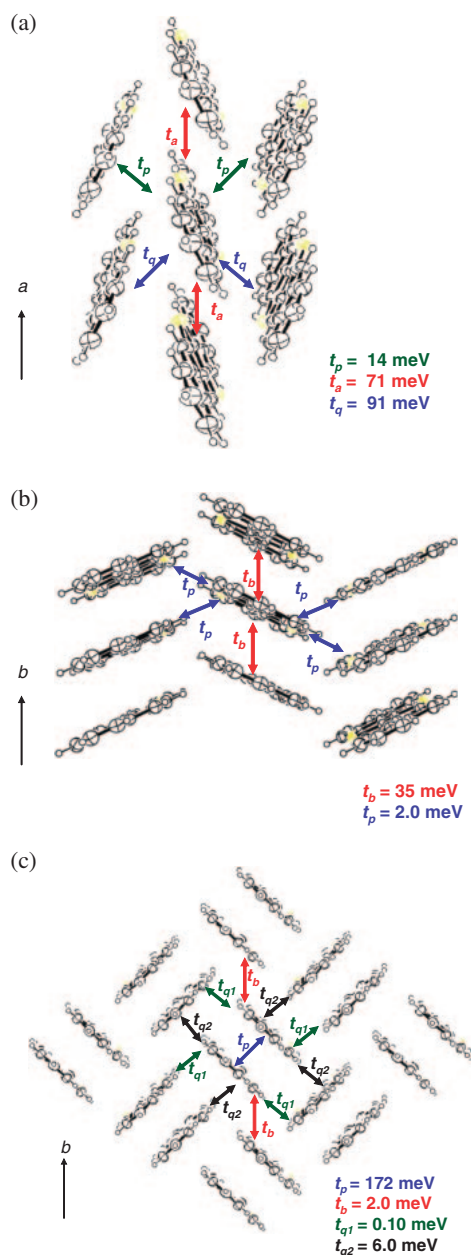


Figure 11. Molecular arrangements and calculated transfer integrals in the semiconducting layer viewed along the molecular long axes of **1** (a), **2** (b), and **3** (c).

Conclusion

In summary, we have synthesized two isomers **2** and **3** of DNTT (**1**), thereby completing the synthesis of all members of the dinaphthothieno[3,2-*b*]thiophene family with C_{2h} symmetry. In the selective synthesis of **2** and **3**, we employed a unique three-step synthesis from naphthaldehyde originally developed for the synthesis of **1**. Characterization of **1**–**3** by means of cyclic voltammetry and UV–vis absorption spectra with the aid of DFT calculations clearly indicated that the molecular electronic structures of the three isomers are different, although they have the same aromatic substructures.

Evaporated thin-film-based OFET devices of **2** and **3** showed typical p-channel FET characteristics but their performance was

very different from that of **1**-based devices. In contrast to the impressive performance of **1**-based OFETs with μ_{FETS} as high as $3.0 \text{ cm}^2 \text{ V}^{-1} \text{ s}^{-1}$, the FET performance of **2**- and **3**-based OFETs was inferior with μ_{FETS} of the order of 10^{-3} – $10^{-2} \text{ cm}^2 \text{ V}^{-1} \text{ s}^{-1}$. In order to clarify such large differences, we focused on the surface morphology of the thin films, the molecular orientation on the substrates, and the molecular arrangements in the solid state. It turned out that the substrate temperatures during thin-film deposition (T_{subS}) had a similar influence on the grain sizes of the thin films of **1**–**3**, whereas the shapes of crystalline grains largely depended on the compound, which may affect the connectivity between crystalline grains. Among the three isomers, the thin film of **1** with dendrite-like morphology reminiscent of the thin-film morphology of pentacene seems to be most suitable for use in the fabrication of high-performance OFETs.

XRD studies of both thin films and single crystals indicated that the molecular arrangements in both states are basically the same and that in the thin-film state, the molecules stand on the surface with their molecular long axes in the surface normal direction. Comparison of the electronic structures of **1**–**3** in the solid state using the single crystal structure indicated that the calculated electronic structures largely depend on the molecular arrangements in the solid state: 2D with large transfer integrals for **1**, 1D with small transfer integrals for **2**, and 2D with small intermolecular transfer integrals for **3**. The FET characteristics of devices based on **1**–**3** were consistent with the electronic structures in the solid state. These experimental as well as theoretical results clearly show that **1** having a highly 2D structure with large intermolecular overlap is most suitable for use in the fabrication of high-performance OFET devices.

The present results indicate that molecular structure and shape, even for molecules with the same molecular formula and symmetry, are crucial parameters to determine the solid-state properties of organic semiconductors. Therefore, careful molecular design taking into account molecular ordering parameters arising from the molecular structure and shape is necessary for the further development of far superior organic semiconductors.

Experimental

General. All chemicals and solvents are of reagent grade unless otherwise indicated. THF was distilled from sodium benzophenone ketyl prior to use. Nuclear magnetic resonance spectra were obtained in deuterated chloroform with a JEOL Lambda 400 spectrometer operating at 400 MHz for ^1H with TMS as internal reference; chemical shifts (δ) are reported in parts per million. EI-MS spectra were obtained on a Shimadzu QP-5050A spectrometer using an electron impact ionization procedure (70 eV). The molecular ion peaks of the compounds showed a typical isotopic pattern, and all the mass peaks are reported based on ^{32}S , unless otherwise stated. Cyclic voltammograms (CVs) were recorded on a Hokuto Denko HA-301 potentiostat and a Hokuto Denko HB-104 function generator in benzonitrile containing tetrabutylammonium hexafluorophosphate (Bu_4NPF_6 , 0.1 M) as supporting electrolyte at a scan rate of 100 mV s^{-1} . Counter and working electrodes were made of Pt, and the reference electrode was Ag/AgCl. All the potentials were calibrated with the standard ferrocene/ferrocenium redox couple ($E^{1/2} = +0.46 \text{ V}$ measured under identical conditions). UV–vis spectra in CH_2Cl_2

solution were recorded on a Shimadzu UV-3100 spectrometer.

2-Methylthio-1-naphthaldehyde (5a).⁸ **Caution!** This procedure involves use of dimethyl disulfide, which emits a powerful stench. Therefore, this must be carried out in a well-ventilated fume hood with disposable gloves.

To a solution of *N,N,N'*-trimethylethylenediamine (2.80 mL, 22.0 mmol) in THF (50 mL) was added butyllithium (13.84 mL of 1.59 M solution in hexane, 22.0 mmol) at -20°C . After the mixture was stirred for 15 min at the same temperature, a solution of 1-naphthaldehyde (**4a**, 2.72 mL, 20.0 mmol) in THF (20 mL) was slowly added over a period of 15 min, and then additional butyllithium (37.74 mL of 1.59 M solution in hexane, 60.0 mmol) was added, and the resulting mixture was stirred for 22 h at -20°C . Excess dimethyl disulfide (7.97 mL, 90.0 mmol) was then added, and after stirring at room temperature for 1 h, 1 M hydrochloric acid (20 mL) was added. The resulting mixture was stirred for 10 h and was extracted with dichloromethane (20 mL \times 3). The combined extracts were dried (MgSO_4) and concentrated in vacuo. The residue was purified by column chromatography on silica gel eluted with hexane–ethyl acetate (9:1, v/v, $R_f = 0.4$) to give **5a** as a yellow solid (2.498 g, 62% isolated yield). Mp $52.0\text{--}53.0^{\circ}\text{C}$; $^1\text{H NMR}$ (400 MHz, CDCl_3): δ 2.62 (s, 3H, SMe), 7.52 (brdd, 1H, $J = 8.7, 8.5$ Hz, ArH), 7.56 (d, 1H, $J = 8.7$ Hz, ArH), 7.64 (brdd, 1H, $J = 8.7, 8.5$ Hz, ArH), 7.84 (brd, 1H, $J = 8.5$ Hz, ArH), 7.99 (d, 1H, $J = 8.7$ Hz, ArH), 8.71 (brd, 1H, $J = 8.5$ Hz, ArH), 11.04 (s, 1H, CHO); $^{13}\text{C NMR}$ (100 MHz, CDCl_3): δ 16.7, 123.0, 123.7, 125.9, 127.2, 128.5, 129.1, 131.0, 132.1, 134.1, 145.7, 190.8; IR (KBr): ν 1668 (C=O), 1544, 1437, 1354, 1191, 1120, 745 cm^{-1} ; EIMS (70 eV): $m/z = 202$ (M^+); Anal. Calcd for $\text{C}_{12}\text{H}_{10}\text{OS}$: C, 71.25; H, 4.98%. Found: C, 71.44; H, 4.96%.

1-Methylthio-2-naphthaldehyde (5b).⁹ **Caution!** This procedure involves use of dimethyl disulfide, which emits a powerful stench. Therefore, this must be carried out in a well-ventilated fume hood with disposable gloves.

To a solution of *N,N,N'*-trimethylethylenediamine (2.87 mL, 21.0 mmol) in THF (35 mL) was added butyllithium (13.2 mL of 1.59 M solution in hexane, 21.0 mmol) at -30°C . After the mixture was stirred for 15 min at the same temperature, a solution of 2-naphthaldehyde (**4b**, 2.0 g, 12.8 mmol) in THF (10 mL) was slowly added over a period of 5 min, and then additional butyllithium (24.15 mL of 1.59 M solution in hexane, 38.4 mmol) was added, and the resulting mixture was stirred for 3.5 h at -30°C . Excess dimethyl disulfide (5.67 mL, 64 mmol) was then added, and after stirring at room temperature for 2 h, 1 M hydrochloric acid (20 mL) was added. The resulting mixture was stirred for 10 h and was extracted with dichloromethane (20 mL \times 3). The combined extracts were dried (MgSO_4) and concentrated in vacuo. The residue was purified by column chromatography on silica gel eluted with hexane–ethyl acetate (9:1, v/v, $R_f = 0.4$) to give **5b** as a colorless solid (0.38 g, 15% isolated yield). Mp $105.0\text{--}106.0^{\circ}\text{C}$; $^1\text{H NMR}$ (400 MHz, CDCl_3): δ 2.45 (s, 3H, SMe), 7.67 (ddd, 1H, $J = 6.8, 6.8, 2.0$ Hz, ArH), 7.70 (ddd, 1H, $J = 7.0, 7.0, 2.6$ Hz, ArH), 7.88–7.92 (m, 2H, ArH), 7.98 (d, 1H, $J = 8.7$ Hz, ArH), 8.82–8.85 (m, 1H, ArH), 11.08 (brs, 1H, CHO); $^{13}\text{C NMR}$ (100 MHz, CDCl_3): δ 21.6, 123.3, 126.8, 127.7, 128.8, 129.1, 129.7, 134.4, 135.9, 136.6, 141.6, 193.5; IR (KBr): ν 1675 (C=O), 1653, 1423, 1315, 1259, 825, 782, 763 cm^{-1} ; EIMS (70 eV): $m/z = 202$ (M^+); Anal. Calcd for $\text{C}_{12}\text{H}_{10}\text{OS}$: C, 71.25; H, 4.98%. Found: C, 71.28; H, 4.87%.

trans-1,2-Bis(2-methylthio-1-naphthyl)ethene (6a). To ice-cooled THF (10 mL), titanium tetrachloride (0.66 mL, 6.0 mL) was slowly added, and the resulting mixture was refluxed for 30 min.

After cooling to room temperature, a solution of **5a** (0.405 g, 2.0 mmol) in THF (5 mL) was added to the mixture, and zinc powder (0.392 g, 6.0 mmol) was added slowly. The resulting mixture was then refluxed for 18 h. After cooling to room temperature, the mixture was diluted with saturated aqueous sodium hydrogen carbonate solution (10 mL) and chloroform (30 mL) and stirred for 1 h. Concentrated HCl solution (10 mL) was added to the mixture, and the mixture was filtered through a filter paper, and the filtrate was separated into an organic and an aqueous layer. The aqueous layer was extracted with chloroform (20 mL \times 3), and the combined organic layer was dried (MgSO_4) and concentrated in vacuo. The residue was purified by column chromatography on silica gel eluted with hexane–ethyl acetate (9:1, v/v, $R_f = 0.6$) to give **6a** as a pale yellow solid (0.182 g, 49% isolated yield). Analytical sample was obtained by recrystallization from dichloromethane. Pale yellow needles; mp $159.0\text{--}160.0^{\circ}\text{C}$; $^1\text{H NMR}$ (400 MHz, CDCl_3): δ 2.59 (s, 6H, SMe), 7.28 (s, 2H, CH=CH), 7.46 (brdd, 2H, $J = 8.3, 7.0$ Hz, ArH), 7.51 (d, 2H, $J = 9.3$ Hz, ArH), 7.55 (brdd, 2H, $J = 8.3, 7.0$ Hz, ArH), 7.81 (d, 2H, $J = 9.3$ Hz, ArH), 7.84 (brd, 2H, $J = 8.3$ Hz, ArH), 8.59 (d, 2H, $J = 8.3$ Hz, ArH); $^{13}\text{C NMR}$ (100 MHz, CDCl_3): δ 16.7, 123.8, 125.2, 125.6, 126.7, 128.0, 128.2, 131.7, 132.0, 132.5, 133.6, 134.8; IR (KBr): ν 1503, 1134, 811, 803, 778, 743 cm^{-1} ; EIMS (70 eV): $m/z = 372$ (M^+), 357 ($\text{M}^+ - \text{Me}$), 325 ($\text{M}^+ - \text{SMe}$); Anal. Calcd for $\text{C}_{24}\text{H}_{20}\text{S}_2$: C, 77.37; H, 5.41%. Found: C, 77.57; H, 5.52%.

trans-1,2-Bis(1-methylthio-2-naphthyl)ethene (6b). To an ice-cooled suspension of zinc powder (0.392 g, 6.0 mmol) in THF (10 mL), titanium tetrachloride (0.66 mL, 6.0 mmol) was slowly added, and the resulting mixture was refluxed for 1.5 h. After cooling to room temperature, a solution of **5b** (0.405 g, 2.0 mmol) in THF (10 mL) was slowly added to the mixture, and the mixture was then refluxed for 20 h. After cooling to room temperature, the mixture was diluted with saturated aqueous sodium hydrogen carbonate solution (30 mL) and chloroform (30 mL) and stirred for 3.5 h. The mixture was filtered through a Celite pad, and the filtrate was separated into an organic and an aqueous layers. The aqueous layer was extracted with chloroform (20 mL \times 3), and the combined organic layer was dried (MgSO_4) and concentrated in vacuo. The resulting residue was purified by passing through a silica gel pad eluted with dichloromethane to give **6b** as pale yellow crystals (0.097 g, 26%). Analytical sample was obtained by recrystallization from dichloromethane. Pale yellow crystals; mp 178.0°C ; $^1\text{H NMR}$ (400 MHz, CDCl_3): δ 2.37 (s, 6H, SMe), 7.51 (dd, 2H, $J = 6.9, 6.9$ Hz, ArH), 7.61 (dd, 2H, $J = 6.9, 6.9$ Hz, ArH), 7.86 (d, 2H, $J = 8.7$ Hz, ArH), 7.88 (d, 2H, $J = 8.7$ Hz, ArH), 8.03 (d, 2H, $J = 8.3$ Hz, ArH), 8.40 (s, 2H, CH=CH), 8.78 (d, 2H, $J = 8.3$ Hz, ArH); $^{13}\text{C NMR}$ (100 MHz, CDCl_3): δ 20.0, 123.9, 126.2, 126.8, 127.2, 128.5, 129.3, 130.6, 133.0, 133.6, 135.2, 139.3; IR (KBr): ν 1503, 1309, 1267, 971, 819, 812, 756 cm^{-1} ; EIMS (70 eV): $m/z = 372$ (M^+), 357 ($\text{M}^+ - \text{Me}$), 325 ($\text{M}^+ - \text{SMe}$); Anal. Calcd for $\text{C}_{24}\text{H}_{20}\text{S}_2$: C, 77.37; H, 5.41%. Found: C, 77.39; H, 5.27%.

Dinaphtho[2,1-*b*:2',1'-*f*]thieno[3,2-*b*]thiophene (2). A solution of *trans*-1,2-bis(2-methylthio-1-naphthyl)ethene (**6a**, 0.062 g, 0.166 mmol) and iodine (1.348 g, 5.312 mmol) in chloroform (5 mL) was refluxed for 27 h. After cooling to room temperature, saturated aqueous sodium hydrogen sulfite solution (10 mL) was added, and the aqueous layer was extracted with chloroform (20 mL \times 3), and the combined organic layer was dried (MgSO_4) and concentrated in vacuo. The residue was purified by column chromatography on silica gel eluted with hexane–dichloromethane

(2:1, v/v , $R_f = 0.7$) and recrystallization with dichloromethane–hexane to give **2** as an off-white solid (0.013 g, 23% isolated yield). Analytical sample was obtained by vacuum sublimation (source temperature: 230 °C under ca. 10^{-3} Pa). Colorless solid; mp >300 °C; $^1\text{H NMR}$ (400 MHz, CDCl_3): δ 7.66 (brdd, 2H, $J = 8.3, 8.3$ Hz, ArH), 7.81 (brdd, 2H, $J = 8.3, 8.3$ Hz, ArH), 7.90 (d, 2H, $J = 8.9$ Hz, ArH), 8.06 (d, 2H, $J = 8.9$ Hz, ArH), 8.07 (brd, 2H, $J = 8.3$ Hz, ArH), 8.59 (brd, 2H, $J = 8.3$ Hz, ArH); IR (KBr): ν 1364, 1225, 903, 790, 732 cm^{-1} ; EIMS (70 eV): $m/z = 340$ (M^+), 170 ($\text{M}^+/2$); Anal. Calcd for $\text{C}_{22}\text{H}_{12}\text{S}_2$: C, 77.61; H, 3.55%. Found: C, 77.66; H, 3.56%.

Dinaphtho[1,2-*b*:1',2'-*f*]thieno[3,2-*b*]thiophene (3**).**⁵ A solution of *trans*-1,2-bis(3-methylthio-2-naphthyl)ethene (**6b**, 0.0814 g, 0.218 mmol) and iodine (1.7706 g, 6.976 mmol) in chloroform (6 mL) was refluxed for 11 h. After cooling to room temperature, saturated aqueous sodium hydrogen sulfite solution (10 mL) was added, and the resulting precipitate was collected by filtration and was washed with water and chloroform to give **3** as a colorless solid (0.0245 g, 33%). Analytical sample was obtained by vacuum sublimation (source temperature: 200 °C under ca. 10^{-3} Pa). Colorless solid; mp >300 °C; $^1\text{H NMR}$ (400 MHz, CDCl_3): δ 7.56–7.59 (m, 2H, ArH), 7.64–7.68 (m, 2H, ArH), 7.90 (d, 2H, $J = 8.7$ Hz, ArH), 7.98–8.01 (m, 4H, ArH), 8.20 (d, 2H, $J = 7.9$ Hz, ArH); IR (KBr): ν 1380, 1322, 1257, 806, 745 cm^{-1} ; EIMS (70 eV): $m/z = 340$ (M^+), 170 ($\text{M}^+/2$); Anal. Calcd for $\text{C}_{22}\text{H}_{12}\text{S}_2$: C, 77.61; H, 3.55%. Found: C, 77.65; H, 3.64%.

X-ray Crystallographic Analysis. Single crystals were obtained by recrystallization from *m*-dichlorobenzene for **2** and from chloroform for **3**. The X-ray crystal structure analysis was made on a Rigaku Rapid-S imaging plate (Mo $K\alpha$ radiation, $\lambda = 0.71069$ Å, graphite monochromator, $T = 296$ K, $2\theta_{\text{max}} = 55.0^\circ$). The structure was solved by the direct method SHELXS. The non-hydrogen atoms were refined anisotropically. Hydrogen atoms were included but not refined. All calculations were performed using the SHELXL-97 package program.²⁴ Crystallographic data for **2** and **3** have been deposited at the Cambridge Data Centre: Deposit numbers CCDC-734667 and -734668, respectively.

Crystal data for **2**: $\text{C}_{22}\text{H}_{12}\text{S}_2$, $M_r = 340.46$, colorless needle, $0.75 \times 0.10 \times 0.05$ mm^3 , Monoclinic, space group $P2_1/c$ (No. 14), $a = 14.3186(16)$, $b = 3.9269(4)$, $c = 13.882(2)$ Å, $\beta = 105.092(6)^\circ$, $V = 753.63(16)$ Å³, $Z = 2$, $D_{\text{calcd}} = 1.500$ g cm^{-3} , $R = 0.044$ for 1712 observed reflections ($I > 2\sigma(I)$) and 109 variable parameters, $R_w = 0.1392$ for all data.

Crystal data for **3**: $\text{C}_{22}\text{H}_{12}\text{S}_2$, $M_r = 340.46$, colorless prism, $0.20 \times 0.15 \times 0.10$ mm^3 , Monoclinic, space group $P2_1/c$ (No. 14), $a = 13.0500(8)$, $b = 8.8641(3)$, $c = 13.6026(6)$ Å, $\beta = 103.239(2)^\circ$, $V = 1531.68(13)$ Å³, $Z = 4$, $D_{\text{calcd}} = 1.476$ g cm^{-3} , $R = 0.051$ for 3519 observed reflections ($I > 2\sigma(I)$) and 265 variable parameters, $R_w = 0.1399$ for all data.

Device Fabrication. Si/SiO₂ substrates were modified as follows. Si/SiO₂ substrate with OTS (octyltrichlorosilane)-SAM (self-assembled monolayer) was obtained by immersing the substrate in 0.1 M OTS in toluene at 60 °C for 20 min.¹⁹ Treatment with HMDS (hexamethyldisilazane) was carried out by exposing silicon wafers to HMDS vapor at room temperature in a closed desiccator under nitrogen for 12 h.²⁰ OFETs were fabricated in the “top-contact” configuration on a heavily doped n⁺-Si(100) wafer with a 200 nm-thick thermally grown SiO₂ ($C_i = 17.3$ nF cm⁻²). A thin film (50 nm thick) of DNTT as the active layer was vacuum-deposited on the Si/SiO₂ substrate maintained at various temperatures (T_{sub}) at a rate of $1\text{--}2$ Å s⁻¹ under a pressure of ca.

2×10^{-3} Pa. On top of the organic thin film, gold films (80 nm) as drain and source electrodes were deposited through a shadow mask. For a typical device, the drain–source channel length (L) and width (W) are 50 μm and ca. 1.5 mm, respectively. The characteristics of the OFET devices were measured at room temperature in air with a Keithley 6430 subfemtoammeter and a Keithley 2400 source meter, operated by a LabTracer program and GPIB interface. Field-effect mobility (μ_{FET}) was calculated in the saturation regime ($V_d = -60$ V) of I_d using the following equation,

$$I_d = (WC_i/2L)\mu_{\text{FET}}(V_g - V_{\text{th}})^2 \quad (2)$$

where C_i is the capacitance of the SiO₂ insulator, and V_g and V_{th} are the gate and threshold voltages, respectively. Current on/off ratio ($I_{\text{on}}/I_{\text{off}}$) was determined from I_d at $V_g = 0$ V (I_{off}) and $V_g = -60$ V (I_{on}). The μ_{FET} data appearing in Table 3 are values from more than 10 different devices.

Theoretical Calculations. Geometry optimization and normal mode MO calculations of **1–3** were carried out by the DFT method at the B3LYP/6-31G(d) level using the Gaussian03 program.¹² The transfer integrals (t) for neighboring molecules in the crystal structures were calculated using the fragment analysis method embedded in Amsterdam Differential Functional (ADF) program with the PW91 functional and Slater-type triple- ζ plus polarization (TZP) basis sets, following the procedure described by Siebbeles et al.²³ and Chao et al.²⁵

This work was partially supported by a Grant-in-Aid for Scientific Research from the Ministry of Education, Culture, Sports, Science and Technology, Japan. Combustion elemental analyses were carried out at the Natural Science Center for Basic Research and Development (N-BARD), Hiroshima University. Computation in the present study was performed with the HPC system PC Grid/Cluster of the Information Media Center, Hiroshima University. We also thank Mr. K. Chiba, Ryoka Systems Inc., Japan for help in the electronic structure calculations with ADF program.

Supporting Information

Molecular arrangement of **1** in the bulk single crystal, AFM images of vapor-deposited films of **1**. This material is available free of charge on the web at <http://www.csj.jp/journals/bcsj/>.

References

- a) D. J. Gundlach, Y. Y. Lin, T. N. Jackson, S. F. Nelson, D. G. Schlom, *IEEE Electron Device Lett.* **1997**, *18*, 87. b) T. W. Kelley, L. D. Boardman, T. D. Dunbar, D. V. Muyres, M. J. Pellerite, T. P. Smith, *J. Phys. Chem. B* **2003**, *107*, 5877.
- a) M. M. Payne, S. R. Parkin, J. E. Anthony, *J. Am. Chem. Soc.* **2005**, *127*, 8028. b) J. E. Anthony, *Chem. Rev.* **2006**, *106*, 5028.
- R. Mondal, R. M. Adhikari, B. K. Shah, D. C. Neckers, *Org. Lett.* **2007**, *9*, 2505.
- a) T. Yamamoto, K. Takimiya, *J. Am. Chem. Soc.* **2007**, *129*, 2224. b) T. Yamamoto, K. Takimiya, *J. Photopolym. Sci. Technol.* **2007**, *20*, 57.
- K. Takimiya, T. Yamamoto, H. Ebata, T. Izawa, *Sci. Technol. Adv. Mater.* **2007**, *8*, 273.
- The synthesis of **3** was already reported, see: M. T. Srinivasa, L. J. Pandya, B. D. Tilak, *J. Sci. Ind. Res., Sect. B* **1961**, *20B*, 169.
- D. L. Comins, J. D. Brown, *J. Org. Chem.* **1984**, *49*, 1078.

- 8 M. S. Korobov, L. E. Nivorozhkin, V. I. Minkin, *J. Org. Chem. USSR* **1973**, *9*, 1739.
- 9 N. P. Buu-Hoï, N. Hoán, D. Lavit, *J. Chem. Soc.* **1953**, 485.
- 10 a) T. Mukaiyama, T. Sato, J. Hanna, *Chem. Lett.* **1973**, 1041. b) J. E. McMurry, *Chem. Rev.* **1989**, *89*, 1513. c) D. Lenoir, *Synthesis* **1989**, 883.
- 11 J. Pommerehne, H. Vestweber, W. Guss, R. F. Mahrt, H. Bäessler, M. Porsch, J. Daub, *Adv. Mater.* **1995**, *7*, 551.
- 12 M. J. Frisch, G. W. Trucks, H. B. Schlegel, G. E. Scuseria, M. A. Robb, J. R. Cheeseman, J. A. Montgomery, Jr., T. Vreven, K. N. Kudin, J. C. Burant, J. M. Millam, S. S. Iyengar, J. Tomasi, V. Barone, B. Mennucci, M. Cossi, G. Scalmani, N. Rega, G. A. Petersson, H. Nakatsuji, M. Hada, M. Ehara, K. Toyota, R. Fukuda, J. Hasegawa, M. Ishida, T. Nakajima, Y. Honda, O. Kitao, H. Nakai, M. Klene, X. Li, J. E. Knox, H. P. Hratchian, J. B. Cross, V. Bakken, C. Adamo, J. Jaramillo, R. Gomperts, R. E. Stratmann, O. Yazyev, A. J. Austin, R. Cammi, C. Pomelli, J. W. Ochterski, P. Y. Ayala, K. Morokuma, G. A. Voth, P. Salvador, J. J. Dannenberg, V. G. Zakrzewski, S. Dapprich, A. D. Daniels, M. C. Strain, O. Farkas, D. K. Malick, A. D. Rabuck, K. Raghavachari, J. B. Foresman, J. V. Ortiz, Q. Cui, A. G. Baboul, S. Clifford, J. Cioslowski, B. B. Stefanov, G. Liu, A. Liashenko, P. Piskorz, I. Komaromi, R. L. Martin, D. J. Fox, T. Keith, M. A. Al-Laham, C. Y. Peng, A. Nanayakkara, M. Challacombe, P. M. W. Gill, B. Johnson, W. Chen, M. W. Wong, C. Gonzalez, J. A. Pople, *Gaussian 03, Revision C.02*, Gaussian, Inc., Wallingford CT, **2004**.
- 13 a) K. Sakanoue, M. Motoda, M. Sugimoto, S. Sakaki, *J. Phys. Chem. A* **1999**, *103*, 5551. b) J.-L. Brédas, D. Beljonne, V. Coropceanu, J. Cornil, *Chem. Rev.* **2004**, *104*, 4971. c) E. F. Valeev, V. Coropceanu, D. A. da Silva Filho, S. Salman, J.-L. Brédas, *J. Am. Chem. Soc.* **2006**, *128*, 9882. d) V. Coropceanu, J. Cornil, D. A. da Silva Filho, Y. Olivier, R. Silbey, J.-L. Brédas, *Chem. Rev.* **2007**, *107*, 926. e) E.-G. Kim, V. Coropceanu, N. E. Gruhn, R. S. Sánchez-Carrera, R. Snoeberger, A. J. Matzger, J.-L. Brédas, *J. Am. Chem. Soc.* **2007**, *129*, 13072.
- 14 R. A. Marcus, *Rev. Mod. Phys.* **1993**, *65*, 599.
- 15 a) V. Coropceanu, O. Kwon, B. Wex, B. R. Kaafarani, N. E. Gruhn, J. C. Durivage, D. C. Neckers, J.-L. Brédas, *Chem.—Eur. J.* **2006**, *12*, 2073. b) G. R. Hutchison, M. A. Ratner, T. J. Marks, *J. Am. Chem. Soc.* **2005**, *127*, 16866.
- 16 a) J. Cornil, J. P. Calbert, J. L. Brédas, *J. Am. Chem. Soc.* **2001**, *123*, 1250. b) H. Yoshida, N. Sato, *Appl. Phys. Lett.* **2006**, *89*, 101919. c) H. Yoshida, K. Inaba, N. Sato, *Appl. Phys. Lett.* **2007**, *90*, 181930. d) S. Schiefer, M. Huth, A. Dobrinevski, B. Nickel, *J. Am. Chem. Soc.* **2007**, *129*, 10316.
- 17 Similar analyses of the crystal structures of polycyclic aromatic hydrocarbons were reported: G. R. Desiraju, A. Gavezzotti, *J. Chem. Soc., Chem. Commun.* **1989**, 621.
- 18 A. Bondi, *J. Phys. Chem.* **1964**, *68*, 441.
- 19 B. S. Ong, Y. Wu, P. Liu, S. Gardner, *J. Am. Chem. Soc.* **2004**, *126*, 3378.
- 20 M.-H. Yoon, S. A. DiBenedetto, A. Facchetti, T. J. Marks, *J. Am. Chem. Soc.* **2005**, *127*, 1348.
- 21 C. D. Dimitrakopoulos, P. R. L. Malenfant, *Adv. Mater.* **2002**, *14*, 99.
- 22 *ADF2008.01*, Scientific Computing & Modeling (SCM), Theoretical Chemistry, Vrije Universiteit, Amsterdam, The Netherlands, <http://www.scm.com>.
- 23 a) K. Senthilkumar, F. C. Grozema, F. M. Bickelhaupt, L. D. A. Siebbeles, *J. Chem. Phys.* **2003**, *119*, 9809. b) P. Prins, K. Senthilkumar, F. C. Grozema, P. Jonkheijm, A. P. H. J. Schenning, E. W. Meijer, L. D. A. Siebbeles, *J. Phys. Chem. B* **2005**, *109*, 18267.
- 24 G. M. Sheldrick, *SHELX-97-Program for the Refinement of Crystal Structures*, University of Göttingen, Germany, **1997**.
- 25 a) M.-Y. Kuo, H.-Y. Chen, I. Chao, *Chem.—Eur. J.* **2007**, *13*, 4750. b) Y.-C. Chang, Y.-D. Chen, C.-H. Chen, Y.-S. Wen, J. T. Lin, H.-Y. Chen, M.-Y. Kuo, I. Chao, *J. Org. Chem.* **2008**, *73*, 4608.